Applied Thermal Engineering 276 (2025) 126938

Contents lists available at ScienceDirect

Applied Thermal Engineering

journal homepage: www.elsevier.com/locate/apthermeng

Research Paper

Design and performance of a ThermoAcoustic Electric Generator powered by waste-heat based on linear and nonlinear modelling☆

Roberto Baccoli [a], Armando Di Meglio [b,*], Antonio Fenu [a], Nicola Massarotti [b]

[a] Institute of Technical Physics, University of Cagliari, Via Marengo 2, 09123 Cagliari, Italy
[b] Engineering Department, University of Naples "Parthenope", Centro Direzionale Napoli, Isola C4 80143, Italy

ARTICLE INFO

Keywords:
Thermoacoustic engine
Travelling wave
Porous media
Oscillatory flows
DeltaEC
OpenFOAM
Pressure drop
Waste heat

ABSTRACT

This article presents the design, numerical modeling, and performance evaluation of a multistage ThermoAcoustic Electric Generator (TAEG), aimed at converting thermal energy from internal combustion engine exhaust gases into electricity. The proposed TAEG adopts a double-stage looped resonator configuration, using helium as the working fluid, with an internal static pressure limited to 20 bar for safety reasons. Gas-to-gas hot heat exchangers were specifically designed to recover waste heat at approximately 530 K. Due to practical constraints, commercial audio speakers were employed as acoustic-to-electric transducers, despite their lower impedance compared to ideal linear alternators.

Initial linear thermoacoustic simulations conducted using DeltaEC software optimized geometric and operational parameters, predicting an electrical power output around 300 W (150 W per stage) with a resistive load of 10 Ω. However, recognizing the inherent limitations of linear modeling, particularly the omission of nonlinear thermo-fluid dynamics, a computational fluid dynamics (CFD) analysis was conducted using OpenFOAM. The CFD model integrated novel nonlinear porous media formulations tailored for oscillatory flow conditions within the thermoacoustic core. Comparisons between a purely linear DeltaEC and OpenFOAM results revealed excellent qualitative agreement but quantitative differences, primarily due to minor losses caused by abrupt geometric discontinuities, and conical segments. A second DeltaEC model including all minor losses based on the steady-state approximation reveals that dissipation were overestimated compared to the CFD model. Therefore, a third DeltaEC model was built by calibrating minor losses based on CFD data. The findings emphasize the critical role of accurately modeling nonlinear effects to reliably predict TAEG performance and the limitation of the local pressure drop coefficients based on steady-state analysis.

1. Introduction

Thermoacoustics is an interdisciplinary field that explores the conversion of thermal energy into acoustic power and vice versa, with potential applications in electricity generation and heating/cooling [1]. This energy conversion occurs due to the presence of a thermal gradient along a carefully designed porous material—commonly referred to as a stack or regenerator (REG) where the heat exchange results in acoustic wave generation, in the case of a thermoacoustic engine. The system also requires at least two Heat eXchangers (HXs) to provide or remove heat, forming the so-called thermoacoustic core together with the REG [2].

There are two primary types of thermoacoustic engines: standing and travelling waves. A standing wave engine relies on a resonant cavity to generate acoustic power, where pressure and velocity oscillations exhibit a phase shift of approximately 90°. In contrast, a travelling wave engine operates with in-phase pressure and velocity oscillations, facilitating a more efficient heat-to-sound conversion process. While standing wave engines design is more straightforward, they are inherently less efficient than travelling wave devices, as they cannot achieve Carnot efficiency due to the heat transfer irreversibility in the stack region [3]. Advancements in thermoacoustic technology have significantly broadened its scope of applications. Notable examples include combustion-driven thermoacoustic systems [4], solar-driven engines [5], and those utilizing supercritical CO_2 [6] which showcase the adaptability of thermoacoustic principles in different energy systems. Recent research has also focused on enhancing design and simulation methodologies. Novel stack configurations, such as pin-array stacks, also with different

☆ This article is part of a special issue entitled: 'HD Oscillating Systems' published in Applied Thermal Engineering.

* Corresponding author.
E-mail address: armando.dimeglio001@studenti.uniparthenope.it (A. Di Meglio).

https://doi.org/10.1016/j.applthermaleng.2025.126938
Received 31 January 2025; Received in revised form 22 May 2025; Accepted 23 May 2025
Available online 25 May 2025

Nomenclature

a	Speed of sound, m/s
A	Area, m^2
c_1, c_2	Coefficients of Darcy-Forchheimer correlations in DeltaEC, –
c_F	Forchheimer coefficient OF, m^{-1}
$\dot{E}$	Acoustic power, W
k_f	Fluid thermal conductivity, W/(mK)
K	Minor loss coefficient
N_t	Number of time steps
p	Pressure
q_{sf}	Volumetric heat source, W/(m^3K)
T	Temperature, K
T	Time, s
U	Volumetric velocity, m^3/s
v	Velocity, m/s
W_{alt}	Electrical power, W
Z	Impedance, Pa s/m or Pa s/m^3

Greek Letters

α	Volumetric heat transfer coefficient, W/m^3K
δ_v	Viscous penetration depth, m
ϕ	Porosity
γ	Specific heat ratio
ρ	density, kg/ m^3
κ	Permeability, m^2
ξ	Acoustic displacement, m
μ	Dynamic viscosity, Pa s

Subscripts

1	First order
0	Static condition
c	Complex
CFD	Computational Fluid Dynamics
h	Hot
r	Radial
z	Axial
alt	Alternator
p	Porous medium

orientations, have been employed to optimize acoustic power generation while minimizing viscous, thermal relaxion and conductive losses [7,8]. Experimental studies have identified optimal configurations, such as the inclusion of energy-matching tubes in heat-driven thermoacoustic heat pumps, improving their coefficient of performance significantly [9]. It is already shown in the available literature that there are several advantages, such as more acoustic power, higher efficiency and lower onset temperature to start-up the engine, if more thermoacoustic cores in multi-stage thermoacoustic engine are connected [10,11]. Zhang et al [12] explored the use of thin-plated surfaces in a multi-stage looped thermoacoustic engine by performing simulations in DeltaEC (Design Environment for Low-amplitude ThermoAcoustic Energy Conversion) software in different configurations. They have shown that adding thin plates enhances sound propagation and increases acoustic power output, improving system performance. Despite these advancements, challenges still exist. The design of HXs remains a bottleneck, due to their dual requirements of minimal thermal dissipation and effective acoustic impedance matching. High pressure differences between thermoacoustic gas and the external input of the heat power source (exhaust gas, heat carrier fluid, solar energy etc.) poses conflicting requirements on material properties that should withstand critical thermomechanical stress and, at once, enhance the efficiency of the heat transfer process, as much as possible. Furthermore, their design is highly challenging because they have to contain at least one peak-to-peak fluid displacement. On the other hand, if such a length is too high, the viscous and thermal dissipation would strongly compromise performance [13,14]. For this reason, in many literature prototypes, the actual hot HX is replaced by an electric resistance heater that can more easily provide the heat input. Electric heaters are very useful for studying fundamental thermoacoustic phenomena, however they do not have practical utility in the actual implementation of a functional thermo-electric energy converter. Some examples of this common practice can be found in refs. [15,16,17]. To this regard, Chen et al. [18] experimentally investigated cooling methods for thermoacoustic engines, including heat pipe HXs. It was found that using heat pipes effectively sustains acoustic oscillations without electricity, proving a viable passive cooling solution. Another issue in the design stage, is the coupling between the thermoacoustic core and the electric transducer in terms of acoustic impedance. Furthermore, the governing equations used for the design (implemented in the tool DeltaEC [19]), do not fully represent the actual working conditions, characterized by strongly nonlinear thermos-fluid-dynamic phenomena. From a modelling point of view, several approaches can be found in the literature to simulate the performance of a thermoacoustic device or one of its components [20]. Generally, DeltaEC is initially employed as a design tool, because it is based on the assumption of 1D problem formulation, and it works on the frequency domain by solving a set of three ordinary differential equations using the shooting method [19]. Linear design tools like DeltaEC often overestimate performance as they neglect nonlinear thermo-fluid-dynamic phenomena, which are not incorporated into the adopted baseline mathematical framework. Nonlinear CFD models, although with a more significant computational cost, provide better insights into real device performance under oscillatory flow conditions. An extensive review work of CFD simulations for thermoacoustic systems can be found in ref. [20]. The motivation for using CFD simulations is to investigate specific nonlinear phenomena, such as minor losses, acoustic streaming, nonlinear stability and bi-stability, which are essential for understanding the actual behavior of thermoacoustic systems [21,22]. However, besides the computational cost of CFD simulations, which is high due to the complexity of solving nonlinear fluid dynamics in the time domain, there is also the challenge of accurately coupling the thermoacoustic system with the electrical transducers. This coupling is much more complex to model compared to simpler 1D or lumped-element models, which can be solved in the frequency domain, unless equivalent impedance boundary conditions are developed [23]. While these simpler models are computationally less expensive and easier to implement, they do not capture the full range of nonlinear effects, particularly at high amplitudes, making CFD simulations necessary for a more accurate analysis. In this article, a (ThermoAcoustic Electric Generator) TAEG is designed by means of DeltaEC software [19] taking into account both the technical limitations to manufacture the Hot Heat Exchangers (HHXs) and considering efficient audio speakers as electric transducers. Additionally, a nonlinear CFD analysis is conducted incorporating a novel nonlinear porous media model operating at oscillatory flow regimes. The results demonstrate that nonlinear effects, particularly those arising from “minor losses”, despite such a misguiding adopted nomenclature, have a significant impact on the device performance at high pressure and velocity regimes. The presented results highlight the differences and similarities between linear and nonlinear modeling approaches. To the best of the authors’ knowledge, this work represents the first effort to compare results from DeltaEC and OpenFOAM (CFD), while maintaining as many consistent operating conditions as possible, given the distinct characteristics of each modeling approach. A purely linear model is developed in DeltaEC (alongside a

first advanced model that incorporates minor losses in which their first order values, are derived from steady state approximation of similar geometries). This comparison is intended to inform forthcoming experimental testing of the prototype.

The rest of the article is organized as follows. In the second section the design criteria of the TAEG are described, while in the third one the analysis based on CFD simulations is shown. Then, the results based on DeltaEC at the design operation point, as well as a sensitivity analysis on the electric load and hot temperature are discussed. Furthermore, CFD results are compared in terms of pressure, velocity and temperature distributions with the previous ones in absence of the alternator. At last, some conclusions are drawn.

2. Design of the prototype

The software 'DeltaEC (Design Environment for Low-amplitude ThermoAcoustic Energy Conversion)' is used to identify a specific configuration of a travelling wave TAEG, with the aim of meeting the following design requirements:

- Internal static pressure $p_0 \leq 20bar$;
- Helium is used as working fluid due to its low Prandl number;
- Exhaust gases, extracted from an internal combustion engine, are used as input of the heat power source and are directly circulated inside the Hot Heat eXchanger (HHX). The hot reservoir temperature is set at $T_h = 530K$;
- Drive ratio, the ratio between the maximum amplitude pressure and the static pressure, $DR = \max(|p_1|)/p_0 \leq 5\%$ according to the validity range of the Rott approximation theory [24];
- Electric power production is targeted to range from $200W$ to $500W$.

The first phase of the investigation focused on the basic design of the active element responsible for converting thermal energy into acoustic energy, which is common to all possible configurations of thermoacoustic generators: the thermoacoustic core. Thus, with the hot reservoir temperature set at $T_h = 530K$ on the HHX and the cold reservoir temperature set at $T_0 = 305K$ in the Ambient Heat eXchanger (AHX), as well as fixing $|p_1| = 100kPa$ at the inlet of the AHX, the theoretical behavior of the thermoacoustic core was analyzed while progressively varying several geometric and thermoacoustic parameters. In particular: the lengths and diameters of the ducts, the porosity of the REG and AHX, the HHX, the oscillation frequency, and the amplitude and phase of the acoustic impedance at the AHX inlet. This was done while prioritizing the maximization of the thermoacoustic conversion efficiency and maintaining constraints on cost and size.

For example, by reducing the oscillation frequency while keeping other parameters constant, an increase in conversion efficiency is generally observed. However, this comes at the cost of an increased longitudinal size of the acoustic circuit (the length doubles for each halving of the frequency). For the present thermoacoustic device, a compromise value was chosen at a frequency $f = 75Hz$.

It is also observed that, under the aforementioned imposed conditions, higher conversion efficiencies are achieved for acoustic impedance values in the REG, on the order of magnitude of approximately $|Z| \approx [10^6, 10^7] Pa \bullet s \bullet m^{-3}$ of amplitude, and $Phase(Z) \approx [-20^\circ, -50^\circ]$ of the phase angle at the inlet of the AHX [25]. This angle varies along the REG, reaching values close to 0° (purely traveling wave) on the side of the HHX. The diameter of the components of the thermoacoustic core is designed based on the desired net acoustic power increase between the inlet and outlet (with respect to the direction of wave propagation) in the REG. Specifically, a value of $\Delta\dot{E} = \dot{E}_{out} - \dot{E}_{in} \approx 1kW$ was assumed in case of a single stage (or equally distributed over more stages) in a such way to obtain an electrical power according the above mentioned objective, after all dissipations in the loop.

Consequently, from the resulting thermal power ($\dot{Q}_h \approx 3kW$ in total) the heat exchange area has been sized by the energy balance, considering a maximum volumetric flow rate of the exhaust gases ($80m^3/h$) allowed by the experimental setup facility. Employing two stages, the final diameter adopted is 154 mm, corresponding to a standard 6-inch pipe with Schedule 40 wall thickness.

The thermoacoustic core was finally completed with the addition of a Thermal Buffer Tube (TBT) and a secondary Ambient Heat eXchanger (AHX#2), with the purpose of insulating the high temperatures of the HHX from the rest of the circuit.

After defining the parameters of the thermoacoustic core, several models were developed to explore different interfacing configurations with the user stages. These models varied in resonator geometry, number of stages, and arrangement of user stages. The quarter-wavelength resonator configuration was discarded due to its excessive size and the large volume of helium required (over $4m$ in length for an operating frequency of $75Hz$). Similarly, a hybrid mechanical-acoustic resonator, while offering compact dimensions, was deemed impractical due to the high costs and development time required for custom moving mass and magnet assembly.

The looped resonator was ultimately chosen as the optimal configuration. It offers reduced size, the ability to accommodate multiple stages, and several advantages, including increased power density, lower operating and onset temperatures for thermoacoustic effects (as supported by previous studies [26,27,28]), and improved heat transfer efficiency. The latter is achieved by using multiple smaller HHXs instead of a single large HHX with equivalent geometry and thermal capacity, resulting in enhanced overall performance [29].

The design efforts were extensively focused on the possible implementation (ultimately unsuccessful, as will be described) of the following two features:

1. Placing the user load (either in series or in parallel) immediately downstream of the thermoacoustic core. This arrangement would allow the net acoustic power gain generated in the REG to be absorbed directly, thereby transferring a smaller portion of the residual acoustic power to the rest of the feedback loop. This, in turn, would proportionally reduce dissipative phenomena within the feedback loop
2. Maintaining a traveling wave (phase close to 0°) throughout the feedback loop, as this minimizes acoustic power losses in the ducts by eliminating the reactive energy component. It also allows for a smaller duct diameter, improving both efficiency and compactness

The cross-sectional area A of the feedback duct can be sized to ensure that a traveling wave at its inlet section, remains traveling during propagation along the same duct. This is achieved by requiring that the magnitude of the specific acoustic impedance $|z| = |p_1|/|u_1|$ (withp_1 = sound pressure [Pa], u_1= oscillating particle speed [m/s]) matches the characteristic impedance of the medium $Z_m = \rho_0 a$ (with ρ_0 = static density [kg/m^3], a = speed of sound [m/s]), under the given static pressure and average working temperature conditions. Both are calculated at the inlet of the feedback tube.

$$|z| = \frac{|p_1|}{|u_1|} = \frac{A|p_1|}{|U_1|}, Z_m = \rho_0 a(T_0) \Rightarrow A = \frac{\rho_0 a(T_0)|U_1|}{|p_1|} \quad (1)$$

Considering that an initial condition, a zero-angle phase must be achieved at the inlet of the feedback duct, corresponding to the outlet of the alternator. This would require the design of a user load stage with an appropriate acoustic impedance Z_{alt}, which could be accomplished using a custom-built linear alternator,that allows for precise control of operating parameters and impedance. However, due to limited resources, standard audio speakers (used in reverse transduction mode compared to their intended design) were chosen instead of purpose-built alternators.

Audio speakers, designed to operate in air at $1atm$, have very low

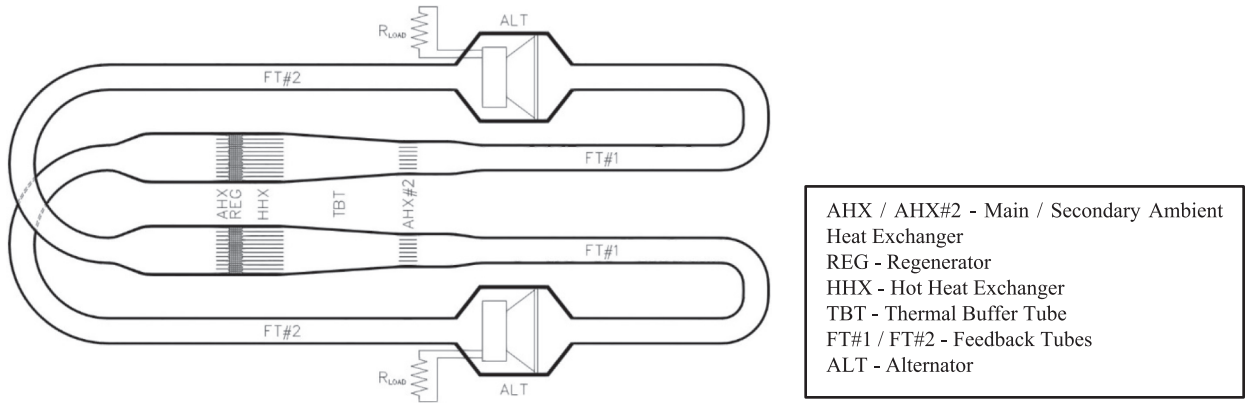

Fig. 1. Sketch of the Two Stage TAEG.

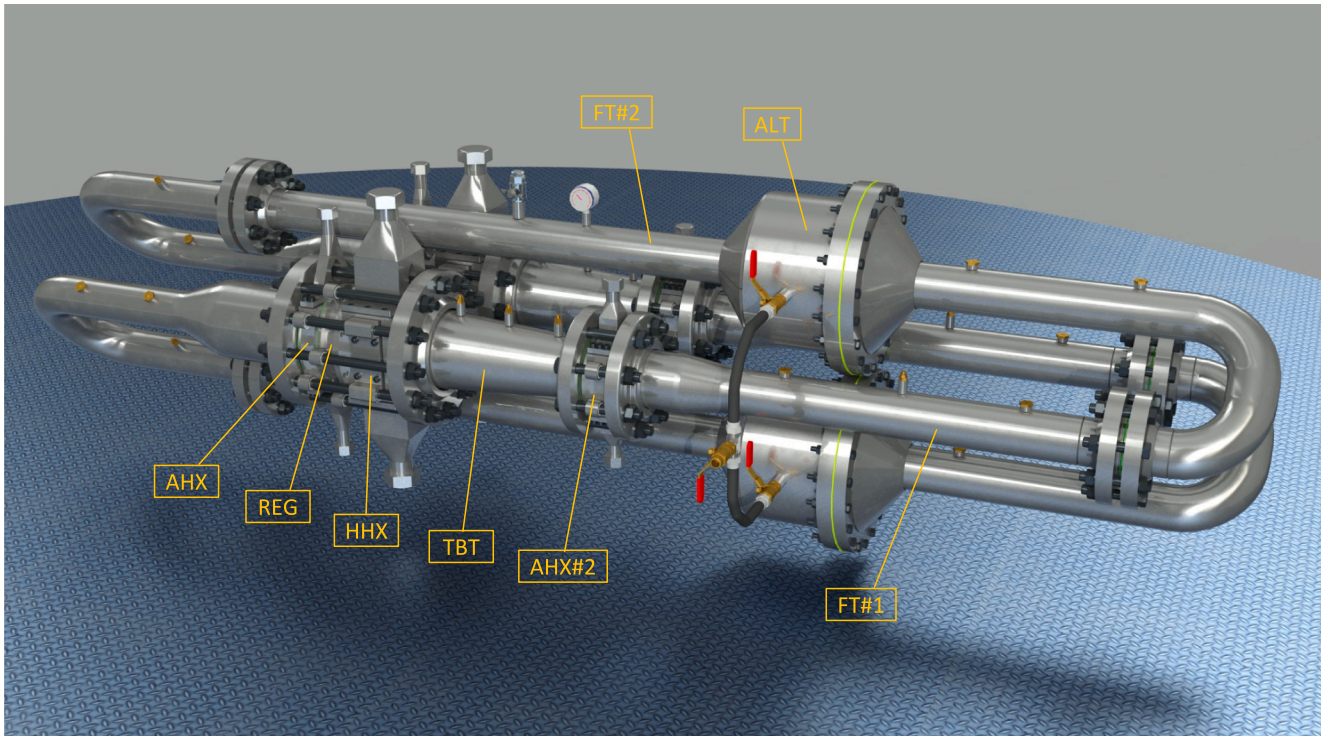

Fig. 2. 3D model of the two-stage TAEG system.

impedance module ($|Z_{alt}| \approx 10^4\, Pa{\cdot}s \bullet m^{-3}$) mainly due to the large diameter of the diaphragm. This makes their direct placement downstream of the thermoacoustic core (characterized by a much higher impedance $|Z| \approx [10^6, 10^7] Pa \bullet s \bullet m^{-3}$) problematic. In a series configuration, they have minimal effect on the incident acoustic wave and fail to produce a purely traveling wave. This is true as the impedance of the incident wave is much higher compared to that of the speaker, so the total impedance, which is the sum of both, is approximately equal to that of the incident wave. Additionally, they are inefficient and subject to significant stress, due to the high differential pressure across the diaphragm.

On the other hand, in a parallel (branch) configuration, the achievement of a traveling wave at the feedback duct inlet would require an impedance to have a high inertance to counterbalance the compliance of the closed branch volume. However, this is not feasible due to the speaker's low impedance and the low moving mass which strongly affects the inertance. As a result, the use of speakers immediately downstream of the thermoacoustic core and the concept of feedback ducts with purely traveling waves had to be abandoned.

The thermoacoustic core-speaker interface was instead resolved by designing looped ducts where the impedance locally decreases to values comparable to that of the speakers, with a phase close to zero.

So, the final design adopted is a two-stage system with a looped resonator and alternators (speakers) arranged in series within the loop, according to the configuration shown in a 2D sketch in Fig. 1 and in a 3D rendering in Fig. 2.

3. Analysis based on CFD simulations

The objective of the CFD simulation is to assess the accuracy of the linearity assumption and investigate similarities and differences with respect to this approach. Nonlinearities, particularly those related to thermo-fluid dynamics, persist even in the absence of an electric load that absorbs the acoustic power generated by the TAEG. Given the complexity to account for the electro-acoustic-mechanical coupling in a CFD-based approach, the authors opted for a study of the thermoa-

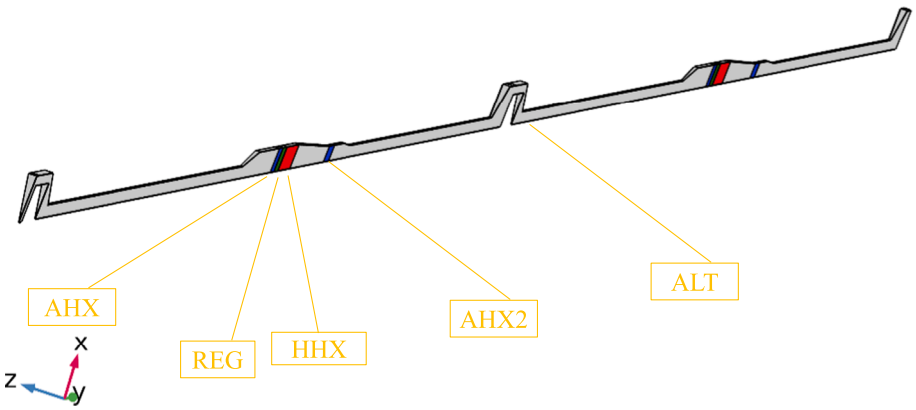

Fig. 3. Computational domain of the CFD model.

Table 1
Boundary conditions of CFD model.

Surfaces	Momentum equation	Energy equation
Inlet/outlet	Cyclic (or periodic)	Cyclic (or periodic)
HHX	No-slip	$T_h = 408K$
AHX1-AHX2	No-slip	$T_0 = 300K$
Wedges	Wedge type ("empty")	Wedge type ("empty")
Other surfaces	No-slip	Adiabatic

coustic engine in absence of the alternator, particularly the diaphragm characterized by its own mass and elasticity. Nevertheless, the footprint of the magnet of the speaker has been considered in the computational domain. Moreover, when the engine operates under no-load conditions, the hot temperature should be reduced up to 408 K, since the amount of acoustic power to be generated should compensate at most for the losses developed due to dissipative thermo-viscous effects, distributed along the thermoacoustic loop. The general governing equations of the thermoacoustic system are the Navier-Stokes equations. The model is assumed to be axisymmetric to reduce computational cost and solved along the radial r and axial x directions. Therefore, the 3D effects given by the bends shown in Fig. 1 for connecting the two stages of the engine have been neglected. The engine can therefore be unrolled and positioned along a single longitudinal axis. In this configuration, the initial and final sections represent the same surface. Continuity, radial-axial momentum components (said v_r, v_z the radial and axial components of the velocity), and energy equations (said E the internal energy) as:

$$\frac{\partial \rho}{\partial t} + \left(\frac{1}{r}\right)\frac{\partial (r\rho v_r)}{\partial r} + \frac{\partial (\rho v_z)}{\partial z} = 0 \tag{2}$$

$$\frac{\partial (\rho v_r)}{\partial t} + \left(\frac{1}{r}\right)\frac{\partial (r\rho v_r v_r)}{\partial r} + \frac{\partial (\rho v_r v_z)}{\partial z} = -\frac{\partial p}{\partial r} + \mu\left[\left(\frac{1}{r}\right)\frac{\partial}{\partial r}\left(r\frac{\partial v_r}{\partial r}\right) + \frac{\partial^2 v_r}{\partial z^2}\right] \tag{3}$$

$$\frac{\partial (\rho v_z)}{\partial t} + \left(\frac{1}{r}\right)\frac{\partial (r\rho v_r v_z)}{\partial r} + \frac{\partial (\rho v_z v_z)}{\partial z} = -\frac{\partial p}{\partial z} + \mu\left[\left(\frac{1}{r}\right)\frac{\partial}{\partial r}\left(r\frac{\partial v_z}{\partial r}\right) + \frac{\partial^2 v_z}{\partial z^2}\right] + S \tag{4}$$

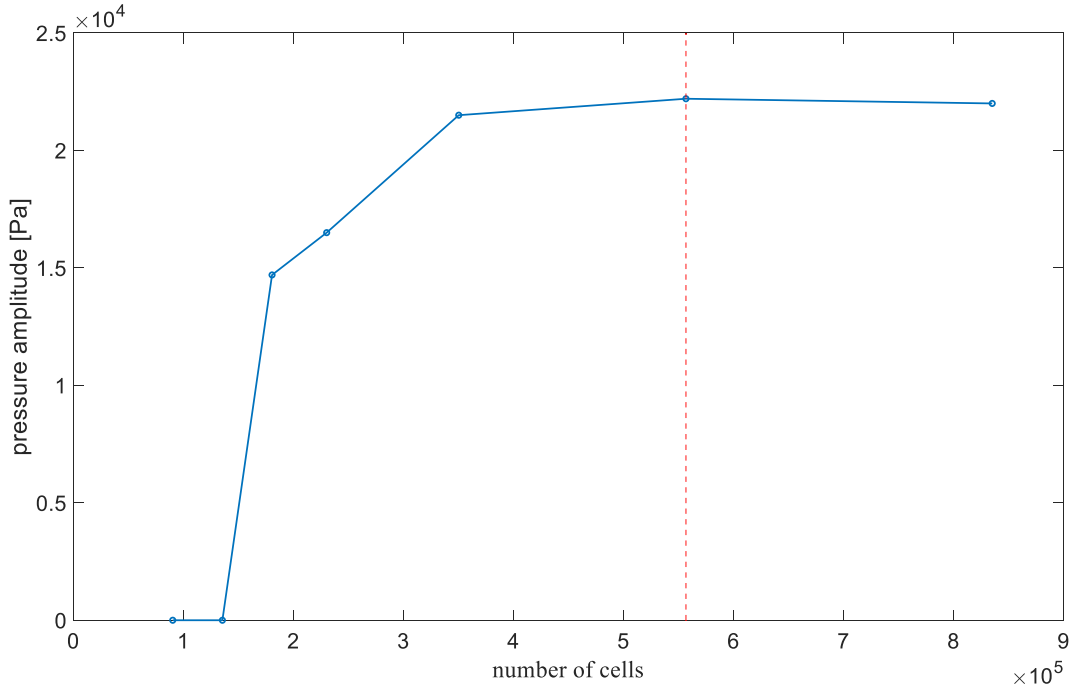

Fig. 4. Mesh sensitivity analysis.

Table 2
Mesh sensitivity analysis, pressure amplitude and % difference between the finest and each mesh.

Number of elements	Pressure amplitude [Pa]	% difference
90,272	0	100 %
135,408	0	100 %
180,544	1.4710^4	33 %
230,194	1.6510^4	25 %
350,231	2.1510^4	2.3
556,726	2.2210^4	0.91 %
835,089	2.2010^4	

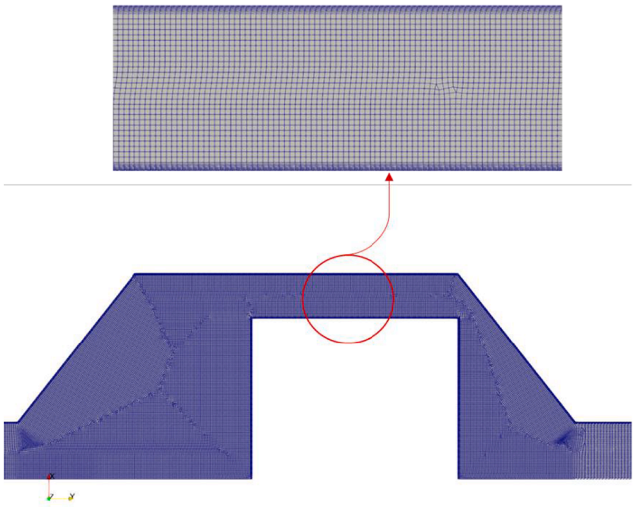

Fig. 5. Selected mesh after sensitivity analysis with a zoom for the boundary layers.

$$\frac{\partial(\rho E)}{\partial t}+\left(\frac{1}{r}\right)\frac{\partial[r(\rho E+p)v_r]}{\partial r}+\frac{\partial[(\rho E+p)v_z]}{\partial z} = \left(\frac{1}{r}\right)\frac{\partial}{\partial r}\left(rk\frac{\partial T}{\partial r}\right)+\frac{\partial}{\partial z}\left(k_f\frac{\partial T}{\partial z}\right)+q_{sf} \tag{5}$$

where p, ρ, T, k, μ are the pressure, density, temperature, thermal conductivity and dynamic viscosity of the working fluid respectively. Density, pressure and temperature are related by the ideal gas law. S and q_{sf} are the source terms for the momentum and energy equations, to represent the microscopic effect of the porous media (regenerators and HXs) on the macroscopic scale. As the pores of the HXs and REGs are characterized by a length scale much shorter than the acoustic wavelength, the two thermoacoustic cores that include six HXs (four cold and two hot) and two REGs have been modelled by means of a porous media approach, at the macroscopic scale [30]. For a travelling wave REG, it was already shown that steady-state correlations for both momentum and energy equations can be successfully applied also in oscillatory flows [20]. In order to be consistent with the model implemented in DeltaEC, the same coefficients for Darcy-Forchheimer have been considered. The corresponding coefficients for the generalized porous media model (permeability κ and Forchheimer coefficient c_F) can be calculated as follows from c_1 and c_2 constants:

$$\kappa=\frac{8r_h^2\phi}{c_1}, c_F=\frac{0.5c_2}{\phi^2 r_h} \tag{6}$$

Permeability and Forchheimer coefficients can be then plugged into the source term of the momentum equation:

$$S_{REG}=-\left(\frac{\mu}{\kappa}u_z+\frac{1}{2}\rho\phi\frac{c_F}{\sqrt{\kappa}}|u_z|u_z\right) \tag{7}$$

Regarding the HXs, whose pores are larger than those of the REGs, they are modelled as a parallel plate porous media, in order to include the nonlinear source and oscillating inertial terms, as explained in more detail in ref. [31]. While there is an analytical formulation for the (complex) permeability needed for the linear viscous and oscillating terms in equation (8), a numerical correlation was built in a previous work [31] for the Forchheimer coefficient c_F, dependent on porosity, frequency and length of the HX:

$$S_{HX}=-\left(\frac{\mu}{\kappa_r}u_z+\frac{\mu}{\omega\kappa_i}\frac{\partial u_z}{\partial t}+\frac{1}{2}\rho\phi\frac{c_F}{\sqrt{\kappa}}|u_z|u_z\right) \tag{8}$$

$$\widetilde{\kappa_c}=\phi\delta_v^2\frac{1-f_v}{2if_v}, \kappa_r=\frac{1}{Re\left\{\frac{1}{\widetilde{\kappa_c}}\right\}}, \kappa_i=\frac{1}{Re\left\{\frac{1}{\widetilde{\kappa_c}}\right\}}, c_F=c_F\left(\phi,\frac{y_0}{\delta_v}\right)\approx 0.02 \tag{9}$$

where $\delta_v^2=2\nu/\omega$ is the viscous penetration depth, y_0 is the half-distance between the fins in the HX.

For the energy equation, a local thermal non-equilibrium model has been adopted to take into consideration the irreversible heat transfer q_{sf} between the solid matrix, considered isothermal at a reference temperature, and the working fluid. The reference temperature for the source term in the energy equation is constant for the HXs, while a linear relation between the hot and cold temperature has been assumed in the REGs:

$$q_{sf}=-\alpha_T(T-T_{ref}), \alpha_T=\frac{k_p}{\gamma r_h^2} \tag{10}$$

where k_p, γ, r_h are the fluid thermal conductivity, specific heat ratio and hydraulic radius of the porous medium.

While in a linear 1D model in DeltaEC it is possible to simulate a single stage of the TAEG, in a CFD-based setup both stages must be included. In the first case, if two stages work perfectly in phase opposition, DeltaEC allows to couple the first and last components of a single stage by constraining equal module and opposite phase of pressure and volumetric flow rate. In the CFD model, unless the exact value of pressure (or velocity) at the beginning and the end of the computational domain are known (this is not the case), this is not allowed, and the complete simulation of the device is required.

A cyclic-periodic boundary condition is applied between the "inlet" and the "outlet" sections of the computational domain pictured in Fig. 3 . The other boundary conditions are all adiabatic no-slip walls, except for the HXs surfaces on which a temperature is applied equal to the cold and hot temperature for all ambient HXs and the hot ones respectively. The type "wedge" boundary conditions have been applied to the surfaces of the revolution domain, as no equations are solved in the azimuthal. The boundary conditions are summarized in Table 1.

The initial conditions are crucial to successfully start-up the engine via the thermoacoustic effect [32]. This is not only a numerical issue, but it also happens in the reality: a thermoacoustic engine needs an initial pulse (for example, by the speaker) to start working. In this case, an entire purely sinusoidal distribution has been applied for the pressure (whose amplitude is $10kPa$) to trigger the thermoacoustic instability. The initial velocity has been set to zero. The initial temperature has been chosen equal to the ambient temperature T_0 apart from the HXs and the REGs in which a constant temperature and linear profile have been considered respectively.

A mesh sensitivity analysis was conducted to confirm that the simulation results are independent of mesh resolution. A mesh comprising approximately 500,000 finite volumes was identified as an optimal balance between computational cost and accuracy. This resolution effectively resolves the viscous and thermal boundary layers. In fact, the selected mesh features finer elements near the walls, with a minimum element size $5{\cdot}10^{-5}m$. This size is based on viscous and thermal penetration depths, calculated as $\sqrt{2\nu/\omega}$ and $\sqrt{2\alpha/\omega}$, (where α

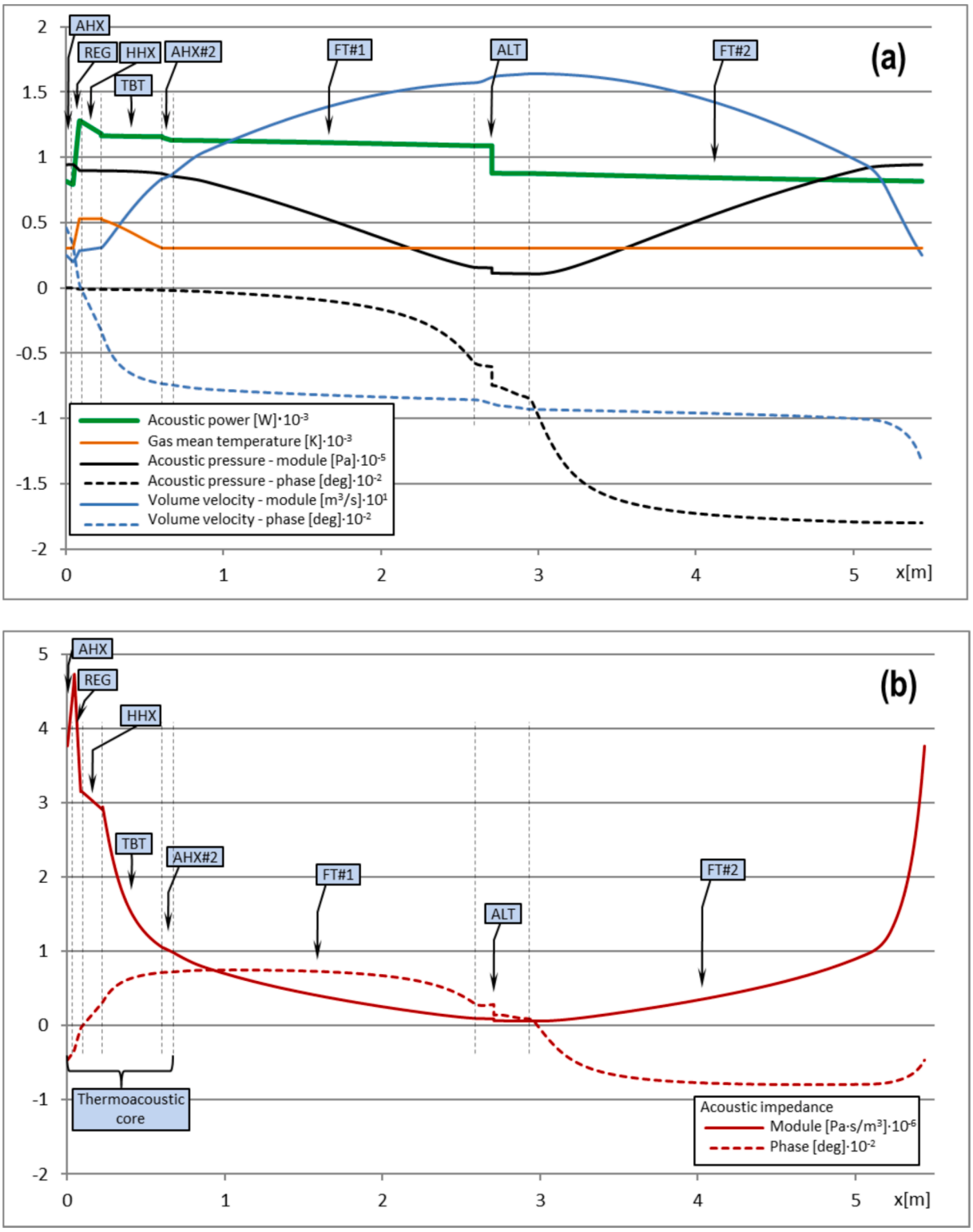

Fig. 6. Distribution of thermoacoustic variables vs x-coordinate for design point.

and ν are the thermal diffusion and kinematic viscosity) which are found to range between $[10^{-4}, 10^{-3}]$ throughout the device.

Finer meshes would notably increase computational effort without significantly affecting the amplitude of the primary variables at the periodic regime. Conversely, coarser meshes fail to reproduce the appropriate thermoacoustic instabilities, as numerical dissipation, combined with viscous and thermal damping effects, dominates the acoustic energy generated by the thermoacoustic phenomena.

Fig. 4 illustrates the results of the mesh sensitivity analysis by plotting the pressure amplitude evaluated at the periodic inlet/outlet boundaries against the number of cells in each analyzed mesh, with a red dashed line highlighting the mesh used for post-processing. As indicated, the initial two meshes, each containing fewer than 200,000 cells, failed to trigger the thermoacoustic effect. Additionally, Table 2 lists the data shown in Fig. 4, alongside the percentage errors computed as the

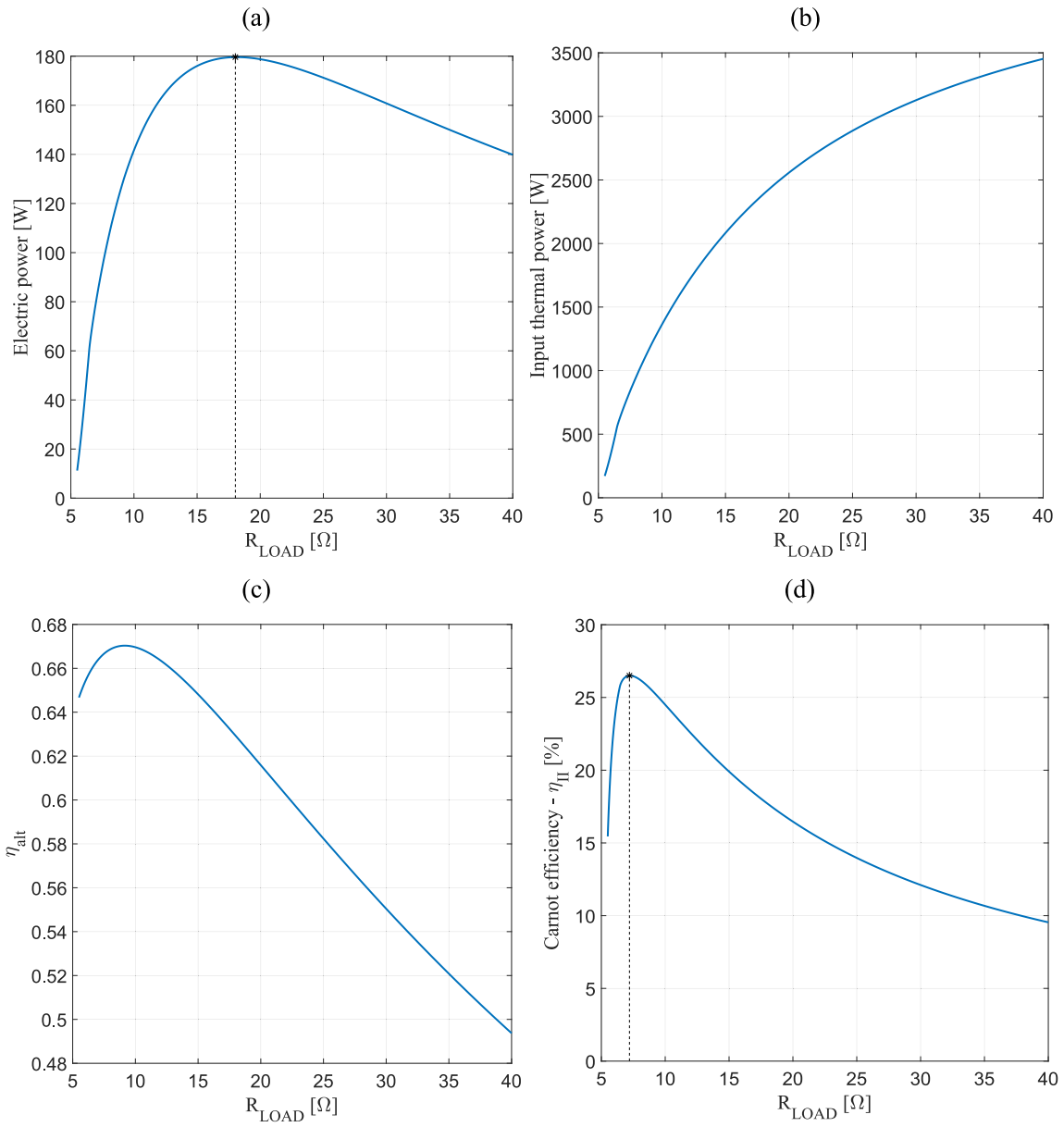

Fig. 7. Single stage electric power (a), input thermal power (b), acoustic-electric efficiency of the alternator (c), Carnot efficiency (d) against the resistive load.

relative difference between results obtained from each mesh and the finest mesh investigated. Finally, Fig. 5 highlights the most critical region of the mesh—the speaker compartment—and provides a zoomed-in view to clearly illustrate the cell distribution near the wall.

The results of this mesh sensitivity analysis align closely with findings reported in similar scientific studies, such as that presented by authors in ref. [22]. In particular, this study utilized the same working fluid (helium) and comparable physical dimensions for the device, making the results comparable. Such a work achieved mesh independence with a lower number of cells, likely because their setup does not include an alternator housing compartment.

The time step of the simulation has been selected based on an adaptive time discretization scheme, with a maximum time step equal to $10^{-5}s$. The CFD simulations were carried out in the open-source software OpenFOAM. The solver configuration in this setup utilizes a preconditioned conjugate gradient (PCG) method for pressure field, with a Diagonal Incomplete Cholesky (DIC) preconditioner and convergence criteria based on absolute tolerance of 10^{-6}). For velocity and internal energy, the PBiCGStab solver with a DILU preconditioner is used, also with a tolerance of 10^{-6}. The PIMPLE algorithm is employed with one outer correction, five inner corrections, and no non-orthogonal correctors, ensuring stability and efficient solution convergence.

4. Results and Discussion

Fig. 6 shows the DeltaEC results in terms of the distribution of the main thermoacoustic variables as a function of the longitudinal spatial coordinate x. DeltaEC assumes one dimensional wave propagation and numerically integrates in one spatial dimension, therefore it is worth remembering that the curves depicted in Fig. 6 are obtained as average values of the whole cross-sectional area at each x coordinate value.

The graph refers to the design operating condition characterized by an oscillation frequency equal to $75Hz$, a hot temperature equal to $T_h = 530K$, the ambient temperature $T_0 = 305K$ and purely resistive load on the alternator $R_{load} = 10\Omega$. The alternator used in the simulation is a commercial audio speaker (model CSW7112 EVO), which has been selected because it has been shown to be more efficient in terms of electro-acoustic transduction, robustness, and maximum diaphragm

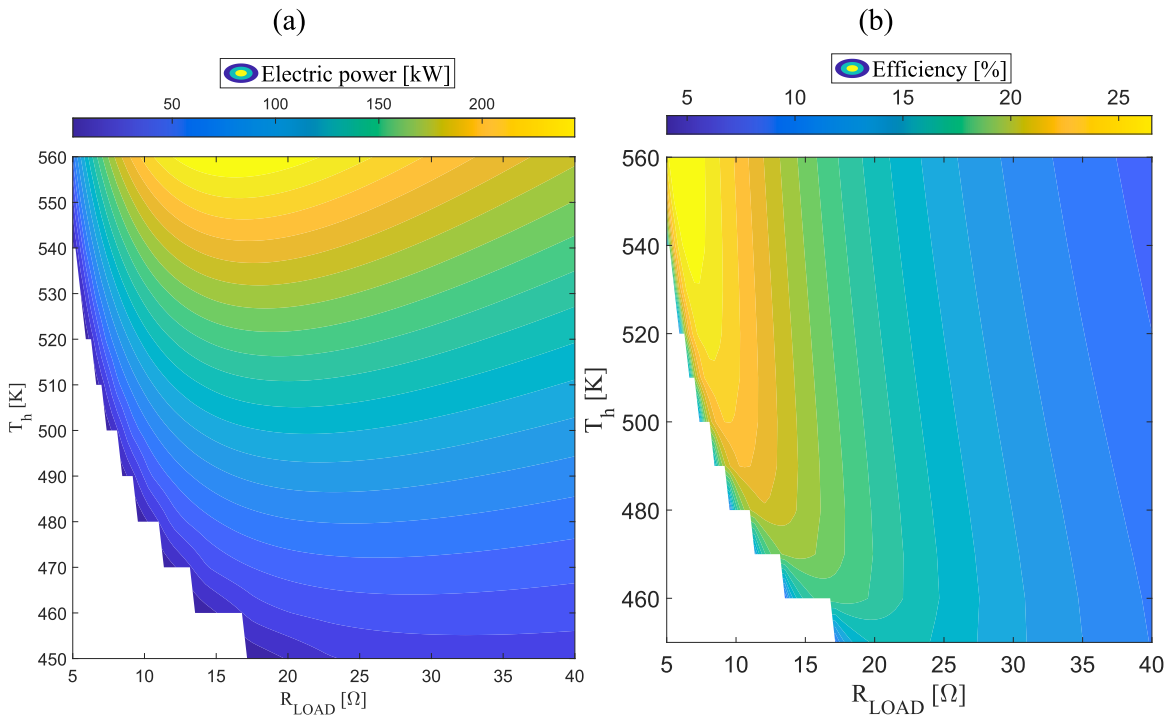

Fig. 8. Sensitivity analysis by varying resistance load and temperature: single stage electric output power (a) and II law Carnot's efficiency (b).

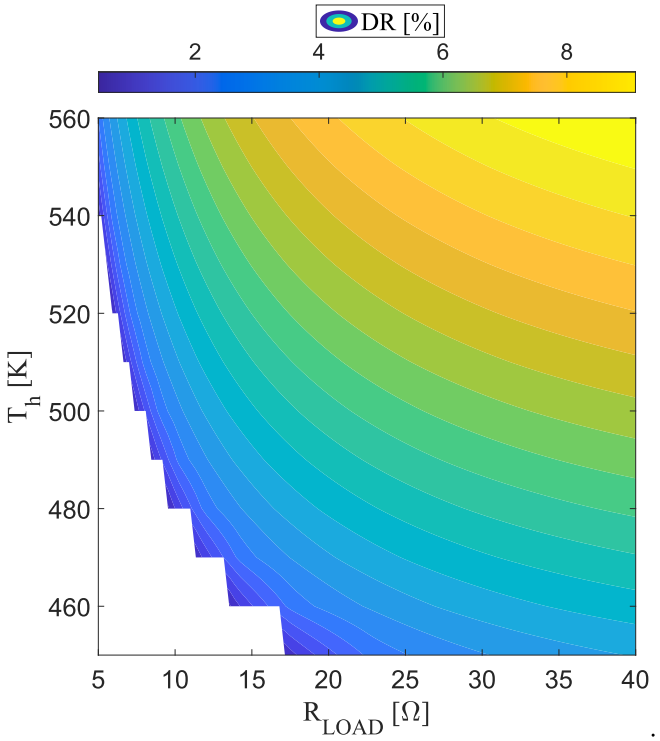

Fig. 9. Drive ratio vs resistive load for different hot temperatures.

amplitude. It must be clarified that only a single stage is illustrated in Fig. 6, as both stages are geometrically identical. The only difference concerns the complex variables (volumetric velocity and sound pressure) which have the same amplitude but opposite phase angle.

The design solution allows us to maintain a high acoustic impedance (with a phase close to 0°) at the thermoacoustic core and a low impedance close to the alternator. This optimal condition was achieved by adopting a feedback duct in which the waves become approximately "standing", with a maximum phase angle in the first feedback tube equal to 75° and minimum of −80° in the second one. As a result, the module of the volume velocity $|U_1|$ is significantly amplified near the alternator, which absorbs from the incident wave an acoustic power equal to:

$$\dot{W}_{alt} = \mathrm{Re}[Z_{alt}]\frac{|U_1|^2}{2} \tag{11}$$

Due to the intrinsic low value of the speaker Z_{alt} impedance, it becomes necessary to significantly enhance the value of the velocity to such an extent that the available acoustic power to be converted into electricity proves to be of adequate high extent (this strategy allows circumventing structural modifications of the alternator).

On the other hand, the drawback is that the larger diameter of the feedback ducts, the higher the reactive acoustic power (and therefore acoustic dissipation and dimensions of the pipes), compared to the case where purely traveling waves were treated.

Nevertheless, dissipation and dimensions are still lower than those of theoretical models developed for configurations with a quarter-wavelength resonator of the same power. The acoustic-electro efficiency of the alternator by which the acoustic power is converted into electricity, is a function of the applied load and is shown in Fig. 7(c):

$$\eta_{alt} = \frac{P_e}{\dot{W}_{alt}} \tag{12}$$

A sensitivity analysis, at the hot and ambient temperature design, has been performed to evaluate how the electric power, heat input (for a single stage) and overall Carnot efficiency change by varying the electrical load of the speaker.

$$\eta_{II} = \frac{P_e}{\dot{Q}_h}\left(1 - \frac{T_0}{T_h}\right) \tag{13}$$

The results are shown in Fig. 7 (a), (b), (d) It is visible that, as in most energy systems, the maximum power operating point does not correspond to the maximum efficiency condition. In fact, the design resistive load was chosen accordingly.

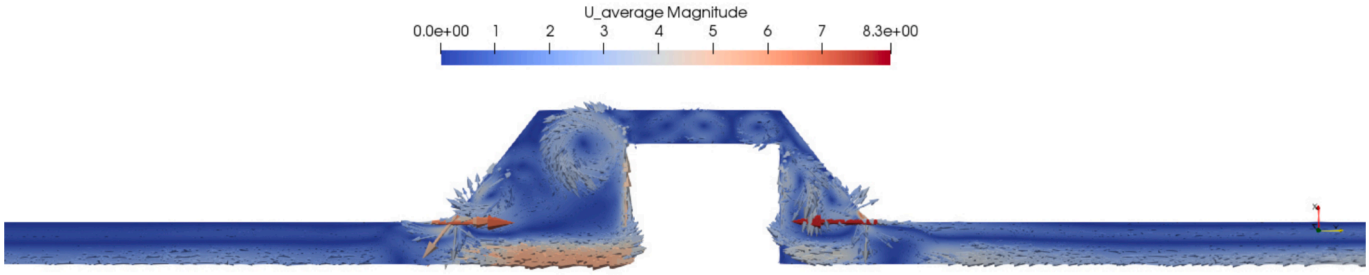

Fig. 10. Example of nonlinear fluid-dynamic structure: steady state velocity field.

A further sensitivity analysis of the thermo-electric efficiency and electric power by varying both hot temperature and resistance load has been conducted, and the results are shown by the contour plots in Fig. 8. From the graphs, it can be observed that at low hot-end temperatures and low load conditions, no operational points of the thermoacoustic engine exist. The operational points, varying with load, increase significantly as the temperature of the hot source rises.

The main limitations of the linear model based on the Rott's equations are summarized in [20]. Overall, as mentioned above, it can be said that DeltaEC results are gradually less reliable beyond a Drive Ratio (DR, the ratio between acoustic pressure and the mean operating pressure) equal to 5–10 %. The contour plot in Fig. 9 shows the relationship between the drive ratio for different operating points by varying the resistive load and the hot temperature source. It can be observed that as the resistive load increases, the temperature required to reach a threshold drive ratio of 5 % (DR = 5 %) decreases.

However nonlinear effects such as the "minor losses" due to geometrical discontinuities, irregularities, conical segments or bends cannot be predicted if the thermoacoustic governing equations are linearized (as they are second order effect in the momentum equation and third order in terms of the energy lost) also at lower DR. In DeltaEC, minor losses can be externally inserted specifying two coefficients, denoted as K^+ and K^-. The strong assumption used to derive the pressure-drop, and therefore the energy loss of the minor loss, is that the classical formula of the local pressure-drop for steady state flow still stands at any instant of time. This is acceptable when the acoustic displacement $|\xi_1|$ (the ratio between the acoustic velocity of the particle and the angular frequency) is much higher than the hydraulic radius r_h. It can be noted that this assumption is conflicting with the assumption based on which the Rott's approximation can be written. The expression of the pressure drop in the frequency domain can be derived by expanding in the Fourier domain the instantaneous pressure drop, according to Swift [3]:

$$\Delta p_1 = \frac{4}{3} K \rho_0 \frac{|U_1| U_1}{A_{min}^2} \tag{14}$$

where $K = 0.5(K^+ + K^-)$, and A_{min} is generally related to the minimum fluid section area involved in the type of "minor loss". K^+ refers to loss in positive direction and K^- in the negative one. The calculation of these coefficients is based on the Idelchik's Handbook of Hydraulic Resistance [33].

To make a fair comparison between a CFD model and the linear description of the TAEG, it is needed to remove the alternator. To do that, the electrical impedance has to tend to a very high value (infinity in theory), while the mass of the magnet and diaphragm (and its properties such as stiffness and mechanical resistance) should approach ideally to zero. However, as already mentioned in the previous section, the space where the magnet is accommodated, over the entire available section, is still considered both in all DeltaEC and CFD models. Moreover, the same temperatures for the HHX and AHX are imposed in DeltaEC as targets, based on the CFD results. This is crucial as the temperature gradient along the REG is the driver of the thermoacoustic effect.

After the initial transient phase, once thermo-fluid-dynamic variables become periodic, data were sampled with a 100 times higher frequency larger both than time step calculation and resonant frequency of the system. Pressure, velocity, and temperature were therefore spatially averaged over the same x-coordinates of the DeltaEC model. In case of temperature, a simple mean time average of the historical profile is calculated while for pressure and velocity the root mean square values are considered.

$$p_{CFD}(x) = \sqrt{2}\sqrt{\frac{1}{N_t}\sum_{i=1}^{N_t} p^2(x, t_i)} \tag{15}$$

$$u_{CFD}(x) = \sqrt{2}\sqrt{\frac{1}{N_t}\sum_{i=1}^{N_t} u^2(x, t_i)} \tag{16}$$

$$T_{CFD}(x) = \frac{1}{N_t}\sum_{i=1}^{N_t} T_{CFD}(x, t_i) \tag{17}$$

The $\sqrt{2}$ factor is needed to adjust it to the peak-value calculated by DeltaEC. The comparisons between DeltaEC and OpenFOAM results are illustrated in Fig. 11, in terms of pressure amplitude, velocity amplitude, impedance (amplitude and phase), acoustic power, temperature. The acoustic power is calculated by averaging the product between pressure and velocity, over an entire period, while the phase angle has been obtained from the acoustic power and the above pressure and velocity root mean square values.

For each variable, three distributions of DeltaEC results are reported. For all of them there is a very good agreement from a qualitative perspective, while from a quantitative point of view there are some differences between the proposed approaches. The red curves represent the minor-losses free case. Based on energy conservation, since no electrical load is considered, the generation due to thermoacoustic effect in the REG is perfectly balanced by the losses. The losses can be due to the viscous dissipation, thermal relaxation and "minor losses".

$$\Delta \dot{E}_{REG} = \Delta \dot{E}_{viscous} + \Delta \dot{E}_{thermal} + \Delta \dot{E}_{minor} \tag{18}$$

If the minor-losses contribution is completely neglected, the balance between generation and dissipation is reached at higher acoustic pressure and velocity.

The yellow curves (in terms of pressure, velocity and acoustic power) represent the case for which all minor losses are considered, and the K's coefficients are evaluated based on the steady-state approximation (conical segments and abrupt cross section variations). It results that, with the same viscous and thermal dissipations, the presence of minor losses is drastically lowering the regime level. Although the qualitative agreement with OpenFOAM results remains excellent, it is evident that the so-called "minor losses" become "major". This is particularly true for the most significant loss in the speaker region, where three minor losses can be identified: two conical segments and sudden contraction–expansion due to the presence of the magnet. The intensity of this loss can be better visualized from Fig. 10, where the average

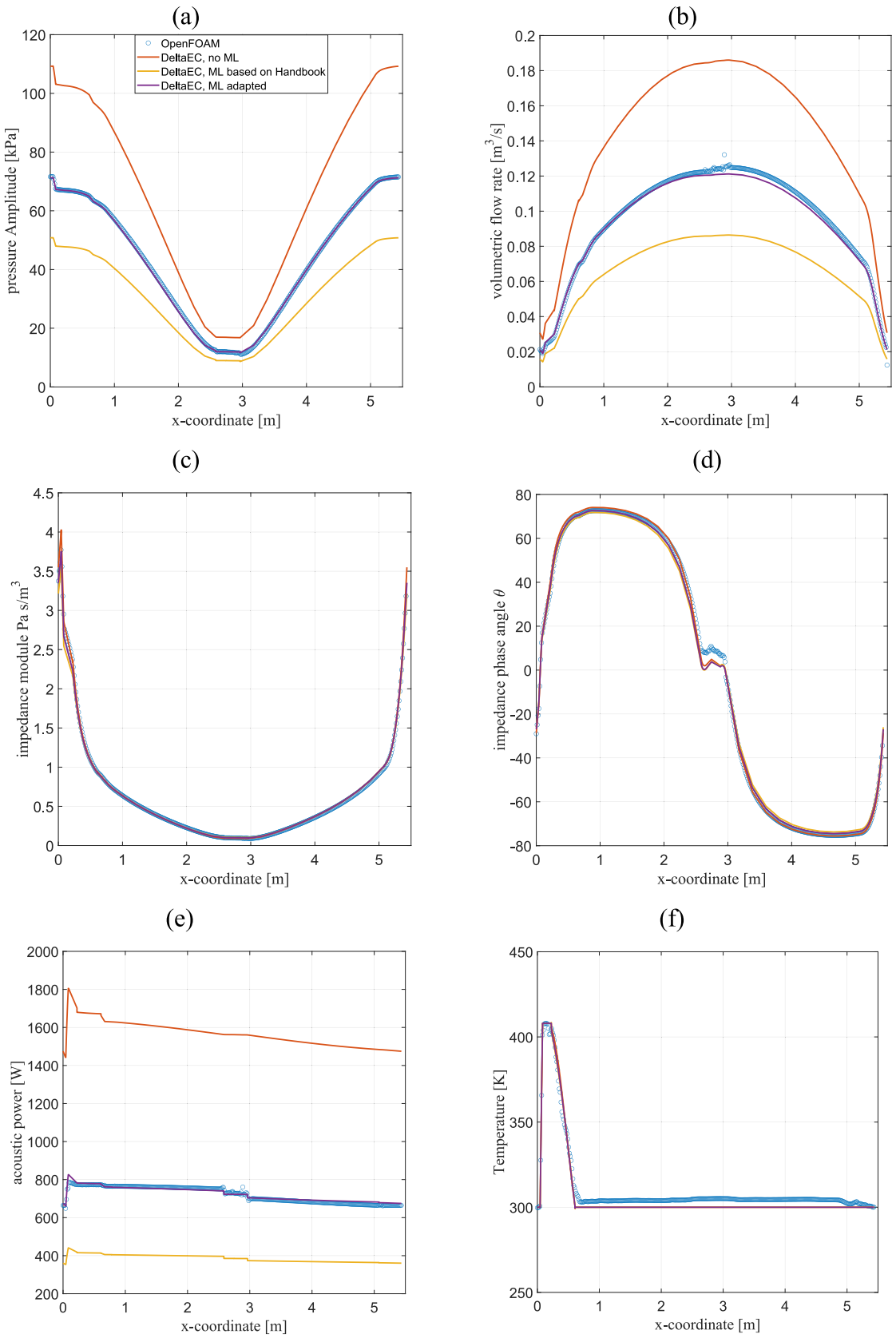

Fig. 11. Comparison between CFD and DeltaEC: pressure amplitude (a), velocity amplitude (b), module impedance (c), phase shift pressure velocity (phase of impedance) (d), acoustic power (e), gas temperature (f) – Open FOAM, DeltaEC with no minor losses, DeltaEC with minor losses based on Idelchik's Handbook of Hydraulic Resistance [33], DeltaEC with minor losses adapted to CFD.

component of the velocity magnitude in the speaker compartment clearly highlights the presence of large and small stationary vortices.

At least three reasons can be identified to justify the difference between CFD and DeltaEC (with all minor losses) results. First of all, it is found that the ratio between the acoustic displacement and the hydraulic ratio ($0.4 \leq |\xi_1|/r_h \leq 3$) is very far from the validity range that Swift proposed ($|\xi_1|/r_h \gg 1$) [3]. Furthermore, the experimental assessment of the loss coefficient in steady-state flows does not take into account the interaction between the local pressure drops. Finally, as it is visible from all phase-shift curves, this loss introduces also a different phase shift between pressure and velocity, increasing the reactive power (the standing component) and decreasing the active acoustic power. Swift [3] warns about the use of such an approach in a range far from validity. Moreover, a single nonlinear viscous loss, as it was proposed by Swift, and re-proposed in present work (by a recalibration of the loss coefficient) may be not enough to represent this kind of losses in a lumped parameter model, especially by neglecting possible effects on the compliance and inertance components of the impedance [3].

As a consequence, the minor losses caused by the speaker compartment have been calibrated based on the CFD results, using the following expression that relates the acoustic power dissipated with the magnitude of the volumetric flow rate.

$$\Delta \dot{E}_2 = \frac{2}{3\pi} \frac{K\rho_m}{A^2} |U_1|^3 \tag{19}$$

This approach clearly shows the best agreement between the DeltaEC model and the OpenFOAM model. Regarding the temperature distributions, to make a fair comparison in terms of energy, it was essential to guarantee the same temperature gradient in the REG, as well as the temperatures of the primary HXs. However, a discrepancy after the TBT of a few degrees between the two approaches is found in the governing equations solved by the two models. The computational thermo-fluidynamic models consider diffusion phenomena in every domain, such as REG, HXs or just feedback tubes. On the other hand, in DeltaEC environment, there is temperature gradient along the main coordinate only in the REGs and HXs and TBTs.

5. Conclusions

This article explores the design and analysis of a double-stage ThermoAcoustic Electric Generator (TAEG). The main focus of this work is on technical constraints and crucial solutions that have been considered and devised for the Hot Heat Exchangers, the coupling between the thermoacoustic core and the electric transducer, and the limit on the operating mean pressure, due to safety and cost reasons. Gas-to-gas Hot Heat Exchangers have been specifically designed to recover waste heat from an internal combustion engine, and audio speakers have been chosen to convert the acoustic power produced by the thermoacoustic core into electricity. Through parametric simulations conducted in the DeltaEC environment, the electric power produced by the device has been found to be around 300 W (150 W per stage) at a hot temperature of 530 K. The model reveals the existence of an optimal value (between efficiency and electricity production) of the electrical resistive load around 10 Ω. The simulation model reveals the existence of a small optimal neighborhood of the electrical resistive load that gravitates around 10 Ω for which the compromise between optimal efficiency and electricity production is achieved. However, it is plausible that some nonlinear effects, not captured by the linear approach adopted by DeltaEC, have been overlooked. To address this, a CFD-based analysis has been conducted to consider these nonlinear effects. CFD simulations conducted at a temperature of 408 K, without considering the electrical load, show that the pressure and velocity data qualitatively align well with the results from DeltaEC. From a quantitative perspective, additional comparisons were made, incorporating all minor losses based on a steady-state approach. The results indicate that some “minor losses” are overestimated when compared to CFD data. A reverse engineering process has been developed on CFD environment for recalibrating the loss factor values to be applied on DeltaEc code. As a result of that adjustment, the CFD and DeltaEC’s output better align. Further analysis of the phase shift between pressure and velocity reveals that the losses within the speaker compartment contribute to the transformation of active power into reactive power. This finding suggests potential future research directions to extract from CFD results not only the equivalent viscous component but also the inertance and compliance, which may be present in real-world applications. Such insights could significantly improve the fidelity of design and performance predictions for thermoacoustic devices, especially when relying solely on DeltaEC software.

Declaration of competing interest

The authors declare that they have no known competing financial interests or personal relationships that could have appeared to influence the work reported in this paper.

Acknowledgement

This research has been partly funded by Italian Ministry of University and Research (MUR): Project number PRIN 2017JP8PHK

Data availability

Data will be made available on request.

References

[1] G.W. Swift, Thermoacoustic engines, *J. Acoust. Soc. Am.* 84 (4) (1988) 1145–1180, https://doi.org/10.1121/1.396617.
[2] G. Chen, L. Tang, B. Mace, Z. Yu, Multi-physics coupling in thermoacoustic devices: A review, Renewable and Sustainable Energy Reviews 146 (May) (2021), https://doi.org/10.1016/j.rser.2021.111170.
[3] G.W. Swift, Thermoacoustics: A Unifying Perspective for Some Engines and Refrigerators. 2017.
[4] W. Xiao, et al., Design and experimental study of a 300 We class combustion-driven high frequency free-piston Stirling electric generator, *Energy* 300 (Aug. 2024), https://doi.org/10.1016/j.energy.2024.131615.
[5] G. Chen, et al., Development of a sunlight-driven thermoacoustic engine for solar energy harvesting, *Appl Therm Eng* 238 (Feb. 2024), https://doi.org/10.1016/j.applthermaleng.2023.122047.
[6] K. Wang, B. Han, H. Peng, Z.C. Hu, Influence of resonator length and temperature configuration on the performance of a supercritical CO2 thermoacoustic engine, *Appl Therm Eng* 250 (Aug. 2024), https://doi.org/10.1016/j.applthermaleng.2024.123462.
[7] E. Di Giulio, A. Di Meglio, N. Massarotti, R.A. Romano, R. Dragonetti, Oriented fibers stacks for thermoacoustic devices, *Appl Energy* 373 (Nov. 2024) 123959, https://doi.org/10.1016/J.APENERGY.2024.123959.
[8] G. Chen, et al., Full-scale numerical simulations of standing-wave thermoacoustic engines with circular-pore and pin-array stacks, *Int J Heat Mass Transf* 228 (Aug. 2024), https://doi.org/10.1016/j.ijheatmasstransfer.2024.125605.
[9] Y. Hu, et al., Study on a high-performance heat-driven thermoacoustic heat pump, *Appl Therm Eng* 253 (Sep. 2024), https://doi.org/10.1016/j.applthermaleng.2024.123790.
[10] J. Xu, et al., A cascade-looped thermoacoustic driven cryocooler with different-diameter resonance tubes. Part II: Experimental study and comparison, *Energy* 207 (2020), https://doi.org/10.1016/j.energy.2020.118232.
[11] J. Xu, J. Hu, E. Luo, L. Zhang, W. Dai, A cascade-looped thermoacoustic driven cryocooler with different-diameter resonance tubes. Part I: Theoretical analysis of thermodynamic performance and characteristics, *Energy* 181 (2019) 943–953, https://doi.org/10.1016/j.energy.2019.06.009.
[12] L. Zhang, H. Kang, X. Ding, Y. Jiang, J. Wen, P. Zhang, Estimation of the effect of thin-plated surface on a three-staged looped thermoacoustic engine for low-grade heat recovery, *Appl Therm Eng* 248 (Jul. 2024), https://doi.org/10.1016/j.applthermaleng.2024.123366.
[13] A. Piccolo, A.J. Jaworski, Experimental study of heat transfer characteristics of finned-tube and circular-pore heat exchangers in oscillatory flow, *Appl Therm Eng* 181 (2020) 116022, https://doi.org/10.1016/j.applthermaleng.2020.116022.
[14] A. Piccolo, Numerical computation for parallel plate thermoacoustic heat exchangers in standing wave oscillatory flow, *Int J Heat Mass Transf* 54 (21–22) (2011) 4518–4530, https://doi.org/10.1016/j.ijheatmasstransfer.2011.06.027.
[15] T. Bi, Z. Wu, W. Chen, L. Zhang, E. Luo, B. Zhang, Numerical and experimental research on a high-power 4-stage looped travelling-wave thermoacoustic electric generator, *Energy* 239 (2022), https://doi.org/10.1016/j.energy.2021.122131.

[16] A. Hamood, A.J. Jaworski, X. Mao, Development and assessment of two-stage thermoacoustic electricity generator, Energies (Basel) 12 (9) (2019), https://doi.org/10.3390/en12091790.
[17] G. Chen, L. Tang, B.R. Mace, Theoretical and experimental investigation of the dynamic behaviour of a standing-wave thermoacoustic engine with various boundary conditions, *Int J Heat Mass Transf* 123 (2018) 367–381, https://doi.org/10.1016/j.ijheatmasstransfer.2018.02.121.
[18] G. Chen, et al., Experimental study on the cooling performances of thermoacoustic heat exchangers, *Int J Heat Mass Transf* 241 (May 2025), https://doi.org/10.1016/j.ijheatmasstransfer.2025.126759.
[19] J.P. Clark, W.C. Ward, G.W. Swift, Design environment for low-amplitude thermoacoustic energy conversion (DeltaEC), *J Acoust Soc Am* 122 (5) (2007) 3014, https://doi.org/10.1121/1.2942768.
[20] A. Di Meglio, N. Massarotti, CFD Modeling of Thermoacoustic Energy Conversion: A Review, Energies (Basel) 15 (10) (2022), https://doi.org/10.3390/en15103806.
[21] L. Guo, et al., Energy conversion performance in looped and stirling traveling-wave and standing-wave thermoacoustic engines, *Appl Therm Eng* 258 (Jan. 2025), https://doi.org/10.1016/j.applthermaleng.2024.124622.
[22] L. Liu, Y. Liu, F. Duan, Effect of the characteristic time on the system performance of a three-stage looped traveling-wave thermoacoustic engine, *Energy Convers Manag* 224 (2020), https://doi.org/10.1016/j.enconman.2020.113367.
[23] F. Guo, J. Du, Y. Wang, Y. Liu, Self-sustained thermoacoustic oscillators with general impedance boundary: Onset and dynamic behavior determination and theoretical–experimental validation, *Appl Therm Eng* 271 (Jul. 2025), https://doi.org/10.1016/j.applthermaleng.2025.126338.
[24] N. Rott, "Thermoacoustics," Adv. Appl. Mech. 20(C), 135–175, 1980. doi: 10.1016/S0065-2156(08)70233-3.
[25] K. Wang, et al., An acoustically matched traveling-wave thermoacoustic generator achieving 750 W electric power, *Energy* 103 (May 2016) 313–321, https://doi.org/10.1016/J.ENERGY.2016.03.001.
[26] T. Jin, R. Yang, Y. Wang, Y. Feng, K. Tang, Low temperature difference thermoacoustic prime mover with asymmetric multi-stage loop configuration, *Sci Rep* 7 (1) (2017) 7665, https://doi.org/10.1038/s41598-017-08124-5.
[27] R. Yang, Y. Wang, T. Jin, Y. Feng, K. Tang, Development of a three-stage looped thermoacoustic electric generator capable of utilizing heat source below 120 °C, *Energy Convers Manag* 155 (Jan. 2018) 161–168, https://doi.org/10.1016/J.ENCONMAN.2017.10.084.
[28] T. Biwa, D. Hasegawa, T. Yazaki, Low temperature differential thermoacoustic Stirling engine, *Appl Phys Lett* 97 (3) (Jul. 2010) 034102, https://doi.org/10.1063/1.3464554.
[29] X. Zhang, J. Chang, S. Cai, J. Hu, A multi-stage travelling wave thermoacoustic engine driven refrigerator and operation features for utilizing low grade energy, *Energy Convers Manag* 114 (Apr. 2016) 224–233, https://doi.org/10.1016/J.ENCONMAN.2016.02.035.
[30] A. Di Meglio, E. Di Giulio, R. Dragonetti, N. Massarotti, A novel model for macroscopic simulation of oscillating heat and fluid flow in porous media, *Int. J. Therm. Sci.* 181 (2022), https://doi.org/10.1016/j.ijthermalsci.2022.107758.
[31] A. Di Meglio, N. Massarotti, S. Rolland, P. Nithiarasu, Analysis of non-linear losses in a parallel plate thermoacoustic stack, *Int J Numer Methods Heat Fluid Flow* 34 (1) (2024) 353–377, https://doi.org/10.1108/HFF-02-2023-0071.
[32] C. Scalo, S.K. Lele, L. Hesselink, Linear and nonlinear modelling of a theoretical travelling-wave thermoacoustic heat engine, *J Fluid Mech* 766 (2015) 368–404, https://doi.org/10.1017/jfm.2014.745.
[33] I.E. Idelchik, *Handbook of hydraulic resistance*, Begell House (2008).